

# Search for light dark matter with ionization signals in the PandaX-4T Experiment

Shuaijie Li,<sup>2</sup> Mengmeng Wu,<sup>3</sup> Abdusalam Abdukerim,<sup>1</sup> Zihao Bo,<sup>1</sup> Wei Chen,<sup>1</sup> Xun Chen,<sup>1,4</sup> Yunhua Chen,<sup>5</sup> Chen Cheng,<sup>3</sup> Zhaokan Cheng,<sup>6</sup> Xiangyi Cui,<sup>2</sup> Yingjie Fan,<sup>7</sup> Deqing Fang,<sup>8</sup> Changbo Fu,<sup>8</sup> Mengting Fu,<sup>9</sup> Lisheng Geng,<sup>10,11,12</sup> Karl Giboni,<sup>1</sup> Linhui Gu,<sup>1</sup> Xuyuan Guo,<sup>5</sup> Chencheng Han,<sup>1</sup> Ke Han,<sup>1</sup> Changda He,<sup>1</sup> Jinrong He,<sup>5</sup> Di Huang,<sup>1</sup> Yanlin Huang,<sup>13</sup> Zhou Huang,<sup>1</sup> Ruquan Hou,<sup>4</sup> Xiangdong Ji,<sup>14</sup> Yonglin Ju,<sup>15</sup> Chenxiang Li,<sup>1</sup> Jiafu Li,<sup>3</sup> Mingchuan Li,<sup>5</sup> Shu Li,<sup>15</sup> Qing Lin,<sup>16,17,\*</sup> Jianglai Liu,<sup>1,2,4,†</sup> Xiaoying Lu,<sup>18,19</sup> Lingyin Luo,<sup>9</sup> Yunyang Luo,<sup>17</sup> Wenbo Ma,<sup>1</sup> Yugang Ma,<sup>8</sup> Yajun Mao,<sup>9</sup> Yue Meng,<sup>1,4,‡</sup> Xuyang Ning,<sup>1</sup> Ningchun Qi,<sup>5</sup> Zhicheng Qian,<sup>1</sup> Xiangxiang Ren,<sup>18,19</sup> Nasir Shaheed,<sup>18,19</sup> Changsong Shang,<sup>5</sup> Xiaofeng Shang,<sup>1</sup> Guofang Shen,<sup>10</sup> Lin Si,<sup>1</sup> Wenliang Sun,<sup>5</sup> Andi Tan,<sup>14</sup> Yi Tao,<sup>1,4</sup> Anqing Wang,<sup>18,19</sup> Meng Wang,<sup>18,19</sup> QiuHong Wang,<sup>8</sup> Shaobo Wang,<sup>1,20</sup> Siguang Wang,<sup>9</sup> Wei Wang,<sup>6,3</sup> Xiuli Wang,<sup>15</sup> Zhou Wang,<sup>1,4,2</sup> Yuehuan Wei,<sup>6</sup> Weihao Wu,<sup>1</sup> Jingkai Xia,<sup>1</sup> Mengjiao Xiao,<sup>14</sup> Xiang Xiao,<sup>3</sup> Pengwei Xie,<sup>2</sup> Binbin Yan,<sup>1</sup> Xiyu Yan,<sup>21</sup> Jijun Yang,<sup>1</sup> Yong Yang,<sup>1</sup> Yukun Yao,<sup>1</sup> Zhengyun You,<sup>3</sup> Chunxu Yu,<sup>7</sup> Jumin Yuan,<sup>18,19</sup> Ying Yuan,<sup>1</sup> Zhe Yuan,<sup>8</sup> Xinning Zeng,<sup>1</sup> Dan Zhang,<sup>14</sup> Minzhen Zhang,<sup>1</sup> Peng Zhang,<sup>5</sup> Shibo Zhang,<sup>1</sup> Shu Zhang,<sup>3</sup> Tao Zhang,<sup>1</sup> Yang Zhang,<sup>18,19</sup> Yingxin Zhang,<sup>18,19</sup> Yuanyuan Zhang,<sup>2</sup> Li Zhao,<sup>1</sup> Qibin Zheng,<sup>13</sup> Jifang Zhou,<sup>5</sup> Ning Zhou,<sup>1,4,§</sup> Xiaopeng Zhou,<sup>10</sup> Yong Zhou,<sup>5</sup> and Yubo Zhou<sup>1</sup>  
(PandaX Collaboration)

<sup>1</sup>*School of Physics and Astronomy, Shanghai Jiao Tong University, Key Laboratory for Particle Astrophysics and Cosmology (MoE), Shanghai Key Laboratory for Particle Physics and Cosmology, Shanghai 200240, China*

<sup>2</sup>*Tsung-Dao Lee Institute, Shanghai Jiao Tong University, Shanghai, 200240, China*

<sup>3</sup>*School of Physics, Sun Yat-Sen University, Guangzhou 510275, China*

<sup>4</sup>*Shanghai Jiao Tong University Sichuan Research Institute, Chengdu 610213, China*

<sup>5</sup>*Yalong River Hydropower Development Company, Ltd., 288 Shuanglin Road, Chengdu 610051, China*

<sup>6</sup>*Sino-French Institute of Nuclear Engineering and Technology, Sun Yat-Sen University, Zhuhai, 519082, China*

<sup>7</sup>*School of Physics, Nankai University, Tianjin 300071, China*

<sup>8</sup>*Key Laboratory of Nuclear Physics and Ion-beam Application (MOE), Institute of Modern Physics, Fudan University, Shanghai 200433, China*

<sup>9</sup>*School of Physics, Peking University, Beijing 100871, China*

<sup>10</sup>*School of Physics, Beihang University, Beijing 102206, China*

<sup>11</sup>*International Research Center for Nuclei and Particles in the Cosmos & Beijing Key Laboratory of Advanced Nuclear Materials and Physics, Beihang University, Beijing 100191, China*

<sup>12</sup>*School of Physics and Microelectronics, Zhengzhou University, Zhengzhou, Henan 450001, China*

<sup>13</sup>*School of Medical Instrument and Food Engineering, University of Shanghai for Science and Technology, Shanghai 200093, China*

<sup>14</sup>*Department of Physics, University of Maryland, College Park, Maryland 20742, USA*

<sup>15</sup>*School of Mechanical Engineering, Shanghai Jiao Tong University, Shanghai 200240, China*

<sup>16</sup>*State Key Laboratory of Particle Detection and Electronics, University of Science and Technology of China, Hefei 230026, China*

<sup>17</sup>*Department of Modern Physics, University of Science and Technology of China, Hefei 230026, China*

<sup>18</sup>*Research Center for Particle Science and Technology, Institute of Frontier and Interdisciplinary Science, Shandong University, Qingdao 266237, Shandong, China*

<sup>19</sup>*Key Laboratory of Particle Physics and Particle Irradiation of Ministry of Education, Shandong University, Qingdao 266237, Shandong, China*

<sup>20</sup>*SJTU Paris Elite Institute of Technology, Shanghai Jiao Tong University, Shanghai, 200240, China*

<sup>21</sup>*School of Physics and Astronomy, Sun Yat-Sen University, Zhuhai, 519082, China*

(Dated: August 29, 2023)

We report the search results of light dark matter through its interactions with shell electrons and nuclei, using the commissioning data from the PandaX-4T liquid xenon detector. Low energy events are selected to have an ionization-only signal between 60 to 200 photoelectrons, corresponding to a mean nuclear recoil energy from 0.77 to 2.54 keV and electronic recoil energy from 0.07 to 0.23 keV. With an effective exposure of 0.55 tonne-year, we set the most stringent limits within a mass range from 40 MeV/c<sup>2</sup> to 10 GeV/c<sup>2</sup> for point-like dark matter-electron interaction, 100 MeV/c<sup>2</sup> to 10 GeV/c<sup>2</sup> for dark matter-electron interaction via a light mediator, and 3.2 to 4 GeV/c<sup>2</sup> for dark matter-nucleon spin-independent interaction. For DM interaction with electrons, our limits are closing in on the parameter space predicted by the freeze-in and freeze-out mechanisms in the early Universe.

Dark matter (DM) direct detection experiments are being carried out worldwide to detect possible interac-

tions between the DM and baryonic matter [1, 2]. DM particles within a mass range from about 5 GeV/c<sup>2</sup> to 10 TeV/c<sup>2</sup> have been extensively searched for via the recoil of atomic nucleus [3–12]. Such DM may have been naturally frozen-out in the early Universe and become the thermal relic [13]. Lighter DM particles are also well-motivated theoretically. In addition to the thermal freeze-out, they could also be produced slowly in non-equilibrium along the evolution of Universe (freeze-in) [14]. Detecting them with conventional techniques, however, becomes more difficult as the recoil energy is much suppressed. Many low threshold techniques have been developed in recent years, enabling experimental searches for the light DM scatterings with nuclei and with shell electrons [15–21]. In this letter, we report a dedicated low threshold search for the light DM particles with ionization-only signals using the commissioning data of PandaX-4T.

The PandaX-4T experiment [12, 22–27] is located in the B2 experimental hall of the China Jinping Underground Laboratory (CJPL). The central detector is a dual-phase Time Projection Chamber (TPC) containing an active cylindrical sensitive target with 3.7 tonnes of liquid xenon (LXe). An energy deposition in LXe produces prompt scintillation photons (*S1*) and ionized electrons in the liquid. Ionized electrons are drifted under the electrical field defined by the cathode and gate grid located at the bottom and top of the LXe, respectively. They are extracted and amplified by a stronger field in between the gate and anode across the liquid level, producing electroluminescence photons (*S2*) proportional to the number of ionized electrons. Both *S1* and *S2* signals are detected by two arrays of Hamamatsu R11410-23 photomultiplier tubes (PMTs) located at the top and bottom of the TPC [12]. For each scintillation photon and ionized electron being produced, the average detection efficiencies are measured to be 9% and 90%, respectively. Therefore, conventional requirement of *S1-S2* pairs inevitably leads to significant efficiency loss for low energy events. Conversely, ionization-only events open up a low energy window down to just a few ionized electrons.

Similar to Ref. [28], a blind analysis is performed on the sets 2 and 4-5 of the commissioning data of PandaX-4T [28]. Data set 3 was removed due to the high micro-discharge noises (MD) from the electrodes. Events with unpaired *S2* (US2), i.e. no accompanying *S1* greater than 2 photoelectrons (PE), are defined as the candidates. The requirement on the accompanying *S1* has an efficiency of >90% for all the DM models probed in this analysis. Data of approximately eight days are randomly selected to validate the signal selection and background composition. The signal selection consists of three steps, the signal reconstruction, the data quality cuts, and the region-of-interest (ROI) selection. The signal reconstruction refers to the identification and reconstruction of the

*S2*-like signals from the raw data. To correctly reconstruct the *S2* signal, PMT hits belonging to an *S2*-like signal are clustered by taking into account the diffusion of the electrons during their drift. Different from previous analyses [12, 28], the *S2* clustering algorithm in this analysis is modified to be solely based on the *S2* charge and width due to the lack of vertical position reconstruction. The data quality cuts are developed based on the calibration data to remove noises and unphysical events, including pile-ups of single-electron events, the background originated from electrodes, events happening in the gaseous region, and MD events. To collect enough statistics of small *S2* signals, the secondary *S2*s from the double scattering (DS) events of the <sup>241</sup>Am-Be and DD calibration are selected. The secondary *S2* is required to precede the main *S2* of the DS events, in order to ensure the purity of the DS sample. Similar to Ref. [28], the data quality cuts are defined based on the *S2* horizontal position reconstruction quality, the top-bottom charge ratio, the signal waveform shape, the veto PMT charge, and the afterglow veto. The data quality cuts (cut0) are further optimized by maximizing signal-to-background ratio, where the background is assumed to consist of solely the so-called cathode background (see later text). For the signal waveform shape cuts, in particular, a selection on *S2* width with *S2*-dependent upper and lower boundaries is adopted, which suppresses the cathode background most significantly.

The *S2* ROI of this analysis is set to be between 60 to 200 PE. The lower boundary of the ROI is determined to avoid the apparent high background rate at very low *S2*, and the upper boundary is set so that the loss of the sensitivity to DM search is negligible (no more than 5% for all the DM models investigated). The “afterglow” veto cut [28] is applied to remove the exposure time with high afterglow *S2* rate. The total effective live time of the selected US2 data is 64.7 days. The same radial cut as in Ref. [12] is also applied, leading to a fiducial mass of  $3.1 \pm 0.1$  tonnes, thus, a total effective exposure of 0.55 tonne-year.

For events located in the ROI, the signal efficiency, separated into the US2 reconstruction efficiency and data quality selection efficiency, is shown in Fig. 1. The US2 reconstruction efficiency is evaluated through dedicated waveform simulation (WS), as described in Ref. [28]. It starts to drop below about 80 PE with an efficiency of about 90% at 60 PE, with negligible systematic uncertainty. The data quality selection efficiency is estimated using the DS and the WS samples [28], and no significant *S2* dependence is observed. Therefore, the average of two methods is taken as the nominal value, and the standard deviation is taken as the systematic uncertainty ( $\sim 31\%$ ).

Prior to the unblinding of the data, three background compositions are evaluated. The electronic recoil (ER) background is primarily due to beta decays of the internal radioactivities such as tritium and <sup>222</sup>Rn. The

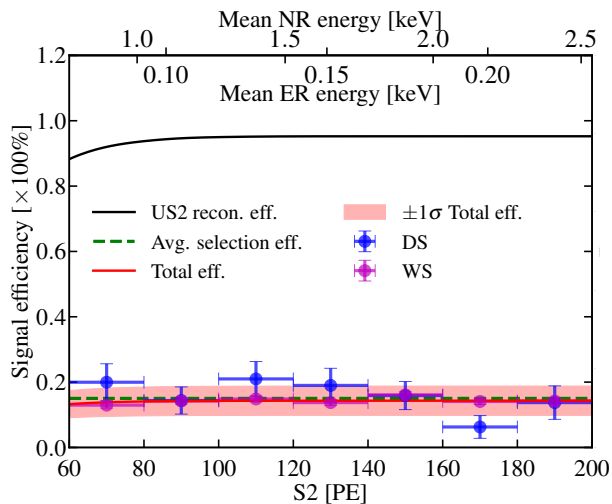


FIG. 1. Total efficiency broken down to US2 reconstruction efficiency (black solid line), and data quality selection efficiencies (green) evaluated using the DS (blue) and WS (magenta) samples. With the data quality selection efficiency modeled as a constant (green dashed line), the total efficiency is shown with  $\pm 1\sigma$  band in light red. The mean NR and ER energy scales in the ROI are indicated on the top axis, which are evaluated based on flat energy spectra.

nuclear recoil (NR) background is produced by the solar  $^8\text{B}$  neutrino elastic scattering off xenon nuclei ( $\text{CE}\nu\text{NS}$ ) and the neutron background. The nominal rates and energy spectra of these backgrounds are the same as those in Ref. [28]. Due to the lack of  $S_1$ , the US2 data are also contaminated by the background emerging from the radioactivities in the cathode or on its surface, exhibiting a signature of  $S_2$  with large width due to diffusion effects [29]. To obtain features of the cathode background, tagged cathode events in  $S_1$ - $S_2$  pairs with characteristic vertical positions are selected. For  $S_1$  less than 100 PE, the  $S_2$  distribution of the selected cathode events is found to be independent of  $S_1$ , and is therefore taken as the shape of the US2 cathode background. The rate of the US2 cathode background is obtained by scaling the tagged cathode events with  $S_2$  in the ROI. The scaling constant is the ratio between the US2 events and tagged cathode events in a side-band with  $S_2$  from 200 to 350 PE and  $S_2$ -width from 2.5 to 4.5  $\mu\text{s}$ . The systematic uncertainty is estimated to be 25%, by varying the side-band region.

A two-step unblinding procedure is carried out on our data to ensure good control over background. In the first step, we define a set of loosened data quality cuts on the US2 width, shape, top/bottom charge ratio etc., and unblind the complementary events (cut1 data) between the loosened cut and cut0, which is more sensitive to instrumental background. The event distribution in cut1 is shown in Fig. 2. Shown on the right panel is the distribution of  $S_2$ -width, which is particularly sensi-

	Nominal	Best-fit
Cathode	$41.6 \pm 10.6$	$63.9 \pm 9.1$
MD	$6.9^{+9.0}$	$17.7 \pm 5.3$
Solar $\nu$	$10.8 \pm 3.7$	$11.7 \pm 3.6$
ER	$2.3 \pm 0.6$	$2.5 \pm 0.5$
Neutron	$0.1 \pm 0.1$	$0.1 \pm 0.1$
Total	$61.7^{+14.4}_{-11.2}$	$95.8 \pm 11.3$

TABLE I. Nominals and background-only best-fits of the background components in the US2 candidates.

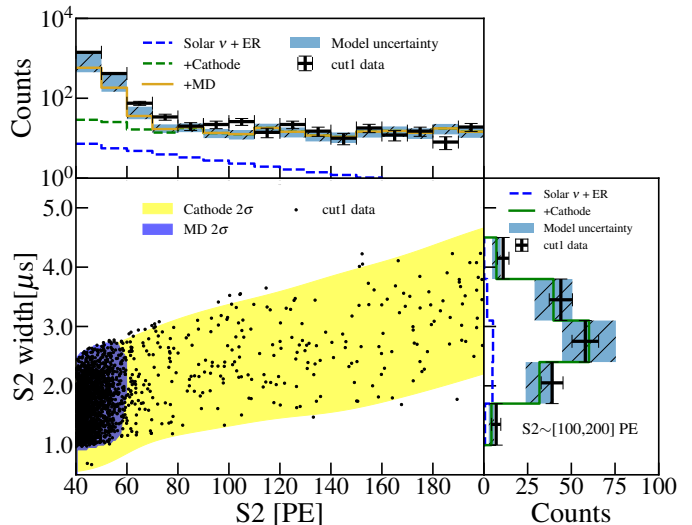


FIG. 2. Main:  $S_2$  width vs.  $S_2$  for events under cut1, together with expected contours of the cathode background (yellow= $2\sigma$ ) and MD background (violet= $2\sigma$ ). Top and right panels: projections to  $S_2$  (all events) and to  $S_2$  width for  $S_2$  within 100 to 200 PE, respectively. Various stacked background components are indicated by the legend, and the background uncertainty is represented by the shaded regions.

tive to cathode background, for events between 100 and 200 PE (nearly no MD contribution). The agreement between the background prediction and the data is good. At the very low- $S_2$  region below 80 PE, a clear excess is observed with a charge and width distributions consistent with the MD in set 3 (excluded already). The rate of the excess also varies with data-taking periods, 1.7 times higher in data sets 4-5 than that in set 2, indicating a residual level of MD after set 3. Therefore, a MD background component is added to the background model for sets 4-5 only, with the rate estimated from the difference between sets 4-5 and set 2 in an  $S_2$  side-band region from 40 to 60 PE [30], and the shape taken from set 3. The comparison between the cut1 data and background prediction is shown in the upper panel of Fig. 2. Our nominal MD background in  $S_2$  [60, 80] PE undershoots the observed cut1 rate by 130%, which may be consistent with a residual MD background component in set 2, or a constant DM signal degenerate with MD background. We assign +130% as an asymmetrical systematic uncer-

tainty for the MD rate in sets 4-5.

The MD prediction under the final cut0 is then set by the MD expectation in Fig. 2 scaled by the ratio of events between cut0 and cut1 in data set 3. The obtained rate and the associated uncertainty of the MD background are listed in Table I (column “nominal”).

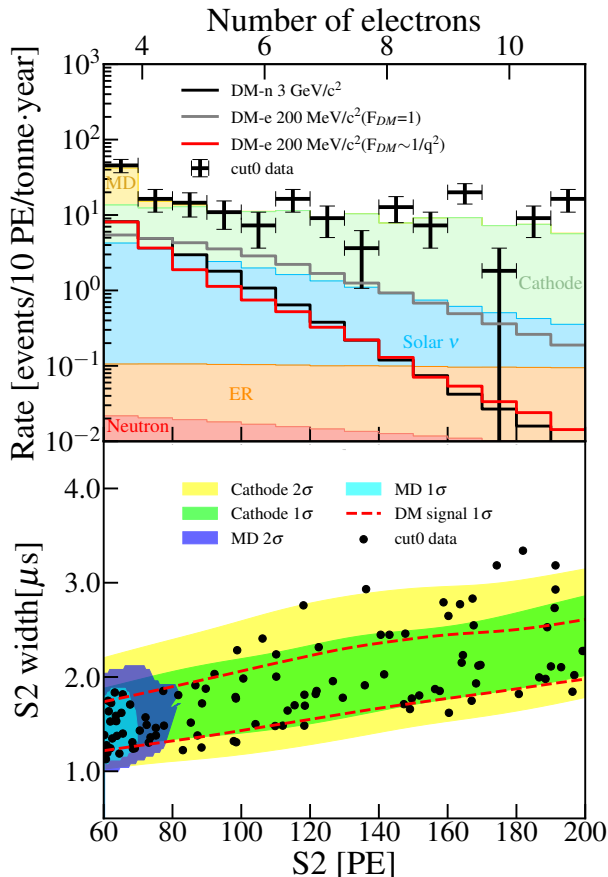


FIG. 3. Top: candidates (cut0) and stacked background components from the background-only best fit. Expected distributions for DM interactions are also overlaid and indicated by the legend, with assumed cross section of  $10^{-43}\text{cm}^2$  (DM-nucleon),  $10^{-41}\text{cm}^2$  (DM-e with  $F_{DM}=1$ ),  $10^{-36}\text{cm}^2$  (DM-e with  $F_{DM} \sim 1/q^2$ ). Bottom: final candidate in  $S2$  width vs.  $S2$  together with the expected contours of the DM signal and the cathode and MD background (see legend).

As in Refs. [12, 28], our NR signal model follow the construction of the NEST package [38], with the parameters obtained from a fit to the PandaX-4T calibration data [12], and extrapolate to our ROI (P4-NEST). The systematic uncertainty is dominated by the charge yield uncertainty in NEST [39] for a recoil energy below  $\sim 5$  keV NR energy. The ER energy scale in the lowest region of the ROI also has large uncertainty as the lowest ever calibration point in LXe is 0.186 keV [40]. Therefore, for the ER events, a more conservative constant- $W$  model [33] is chosen as the nominal model. The ROI corresponds to the mean energy range from 0.77

to 2.54 keV for NRs (P4-NEST), and 0.07 to 0.23 keV for ERs (constant- $W$ ). The solar  $\nu$ , ER and neutron background can then be estimated under these models (Table I). The surface background is negligible within the FV cut.

Nuisance parameters	Stdev.	Estimated by	
Data sel. eff.	$\delta_\epsilon$	0.31	DS vs. WS
Sig. model rate	$\delta_s f_i$	$f_i$	NEST uncert.
Cathode bkg. rate	$\delta_{\text{cat}}$	0.25	ROI side-band
MD bkg. rate	$\delta_{\text{MD}}$	+1.3 -0.0	cut1 data

TABLE II. Summary of the standard deviations of the nuisance parameters (nominal values all at 0) used in the statistical interpretation (see text).  $f_i$  is an correlated energy-dependent fractional uncertainty of the DM signal rate in each  $S2$  bin.

The second step unblinding happens after all background nominals in the ROI are set. In total 105 events are observed in cut0, shown in Fig. 3. Statistical interpretation of the US2 data is performed based on a two-sided profile likelihood ratio (PLR) method [41]. The binned likelihood of this analysis is defined as:

$$\mathcal{L} = G(\delta_\epsilon)G(\delta_s)G(\delta_{\text{cat}})G(\delta_{\text{MD}}) \prod_i \frac{\lambda_i^{N_i}}{N_i!} e^{-\lambda_i}, \quad (1)$$

where  $N_i$  and  $\lambda_i$  are the observed and predicted events, respectively, in the  $i$ -th bin in  $S2$ .  $\delta_\epsilon$ ,  $\delta_s$ ,  $\delta_{\text{cat}}$ , and  $\delta_{\text{MD}}$  are the nuisance parameters corresponding to the systematic uncertainties of the data selection efficiency, the DM signal rate, the cathode background rate, and the MD background rate, respectively, constrained by Gaussian terms  $G$  (see also Table II). The expected events  $\lambda_i$  can be written as:

$$\lambda_i = N_i^X (1 + \delta_s f_i) (1 + \delta_\epsilon) + N_i^{\text{cathode}} (1 + \delta_{\text{cat}}) + N_i^{\text{MD}} (1 + \delta_{\text{MD}}) + N_i^{\text{others}}, \quad (2)$$

where  $N_i^X$ ,  $N_i^{\text{cathode}}$ ,  $N_i^{\text{MD}}$ , and  $N_i^{\text{others}}$  are the nominal events for the DM signals, cathode background, MD background, and other background (solar  $\nu$ , ER, and neutrons), respectively. The DM signal and background models for set 2 and sets 4-5 are generated separately according to their detector conditions and then summed up. The parameter  $\delta_s$  is factored together with a fractional shape uncertainty  $f_i$  which depends on actual DM signal spectrum, similar to Ref. [28]. For example, for a point-like 200 MeV/c<sup>2</sup> DM-electron interaction,  $f_i$  varies from 1% to 37% from 60 to 200 PE. The background-only best-fit rates of the background components are summarized in Table. I. An upward shift is observed in the cathode background, nevertheless within two standard deviations from the nominal, which is conservative in the case of setting exclusion limits. No significant excess is observed above expected background, therefore our data are cast

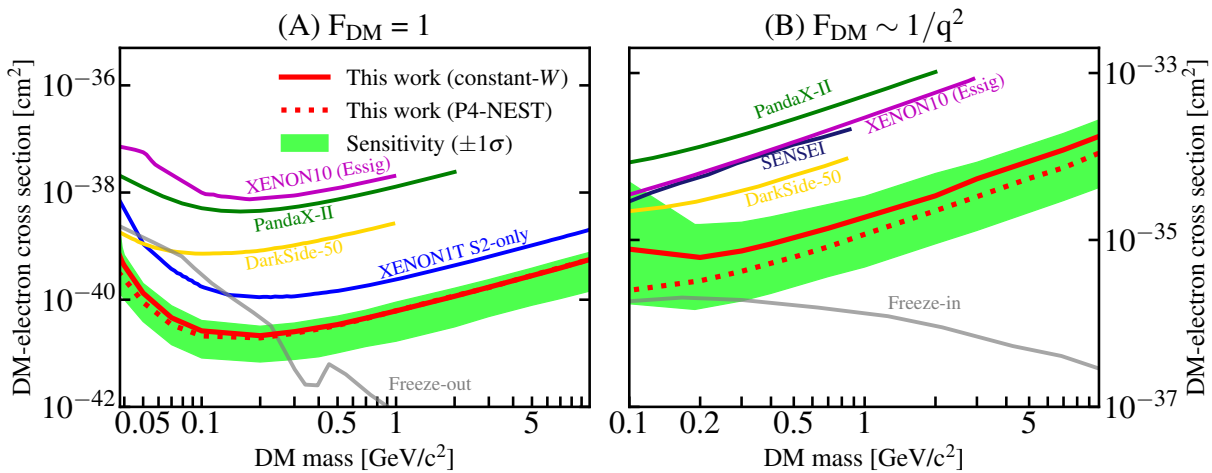


FIG. 4. The 90% C.L. upper limits on DM-electron cross sections of the point-like interaction with  $F_{\text{DM}} = 1$  (left panel) and with the light mediator with  $F_{\text{DM}} \sim 1/q^2$  (right panel) using the constant- $W$  model (red solid, official results) and P4-NEST model (red dashed), as well as the green  $\pm 1\sigma$  sensitivity band. For comparison, results from other experiments [15, 18, 31–34], as well as theoretical predictions from DM vector-portal freeze-in and freeze-out mechanisms ( $\Omega h^2 = 0.12$ ) [20], are also overlaid.

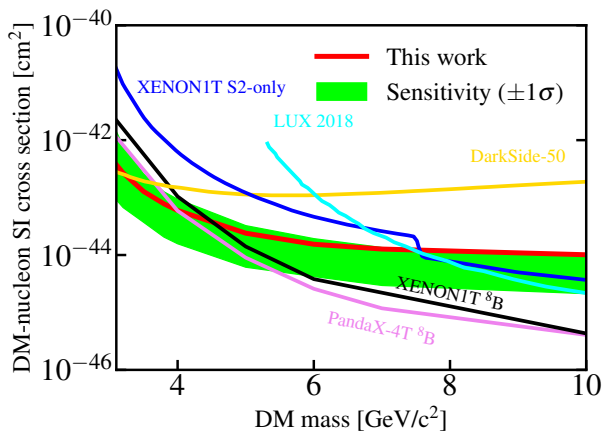


FIG. 5. The 90% C.L. exclusion limit on the spin-independent DM-nucleon cross section with  $\pm 1\sigma$  sensitivity, together with results from other work [28, 33, 35–37].

into DM exclusion limits. The  $2\sigma$  upward shift in the fitted cathode background implies an underestimation of the background, but is nevertheless conservative in the case of limit setting. Likewise, our nominal MD background and its asymmetric uncertainty also lead to a more conservative limit.

Three benchmark models are considered in this analysis: the DM-electron elastic scatterings with a heavy mediator (the DM form factor  $F_{\text{DM}} = 1$ ) and a light mediator ( $F_{\text{DM}} \sim 1/q^2$ , where  $q$  is the momentum transfer) [33], and the DM-nucleon spin-independent (SI) scattering. The exclusion limits on the scattering cross-sections at 90% C.L. are shown in Fig. 4 and Fig. 5. To set the scale, the limits are about  $1.3 \times 10^{-43} \text{ cm}^2$  ( $3.5 \text{ GeV}/c^2$ ) for the DM-nucleon SI scat-

tering and  $2.1 \times 10^{-41} \text{ cm}^2$  ( $200 \text{ MeV}/c^2$ ) for DM-electron scattering with a heavy mediator. The obtained results have provided the most stringent constraints for the DM-electron interactions with mass in range of  $40 \text{ MeV}/c^2$  to  $10 \text{ GeV}/c^2$  with  $F_{\text{DM}} = 1$ , and  $100 \text{ MeV}/c^2$  to  $10 \text{ GeV}/c^2$  with  $F_{\text{DM}} \sim 1/q^2$ , and for DM-nucleon SI interactions in the DM mass range of  $3.2$  to  $4 \text{ GeV}/c^2$ . Results with lower DM masses are not reported, as the sensitivity band grows significantly due to the large systematic uncertainty on the charge yields. Our exclusions on DM-electron interactions represent a significant step-forward in the field. Under the assumption of vector portal interactions (e.g. the dark photon as the mediator), our results challenge the freeze-out mechanism for DM mass range from  $0.04$  to  $0.25 \text{ GeV}/c^2$  with  $F_{\text{DM}} = 1$ , and are closing in on the freeze-in prediction with  $F_{\text{DM}} \sim 1/q^2$ , assuming such light DM provides the entire DM abundance.

In summary, a blind analysis using ionization-only data from the PandaX-4T commissioning run is carried out to search for light DM interactions with xenon nuclei and atomic electrons. We have lowered the  $S2$  threshold to 60 PE, equivalent to a mean NR energy of about  $0.77 \text{ keV}$  and ER energy of about  $0.07 \text{ keV}$ . All background components in the ROI are understood and well constrained. With an effective exposure of  $0.55 \text{ tonne-year}$ , no significant excess is observed above background. Thus, we have obtained the leading constraints on the DM-electron cross-sections with the DM mass in the range of  $40 \text{ MeV}/c^2$  to  $10 \text{ GeV}/c^2$  for a heavy mediator, and  $100 \text{ MeV}/c^2$  to  $10 \text{ GeV}/c^2$  for a light mediator, respectively, and on the DM-nucleon SI cross-sections within the DM mass range from  $3.2$  to  $4 \text{ GeV}/c^2$ . PandaX-4T is taking more physics data and

working to suppress the background further, aiming to further improve the sensitivity with a 6-tonne-year total exposure.

We would like to thank Matthew Szydagis for useful discussions concerning NEST model uncertainty. This project is supported in part by grants from National Natural Science Foundation of China (Nos. 12090061, 12005131, 11905128, 11925502, 12222505, 11835005), a grant from the Ministry of Science and Technology of China (No. 2016YFA0400301), and by the Office of Science and Technology, Shanghai Municipal Government (grant No. 18JC1410200). We thank supports from Double First Class Plan of the Shanghai Jiao Tong University. We also thank the sponsorship from the Hongwen Foundation in Hong Kong, Tencent Foundation in China, and Yangyang Development Fund. Finally, we thank the CJPL administration and the Yalong River Hydropower Development Company Ltd. for indispensable logistical support and other help.

---

\* Corresponding author: qinglin@ustc.edu.cn

† Spokesperson: jianglai.liu@sjtu.edu.cn

‡ Corresponding author: mengyue@sjtu.edu.cn

§ Corresponding author: nzhou@sjtu.edu.cn

- [1] J. Liu, X. Chen, and X. Ji, *Nature Phys.* **13**, 212 (2017).
- [2] T. M. Undagoitia and L. Rauch, *Journal of Physics G: Nuclear and Particle Physics* **43**, 013001 (2015).
- [3] A. Tan *et al.* (PandaX), *Phys. Rev. D* **93**, 122009 (2016).
- [4] E. Aprile *et al.* (XENON), *Phys. Rev. Lett.* **121**, 111302 (2018).
- [5] D. Akerib *et al.* (LUX), *Phys. Rev. Lett.* **118**, 021303 (2017).
- [6] P. Agnes *et al.* (DarkSide), *Phys. Rev. D* **98**, 102006 (2018).
- [7] R. Ajaj *et al.* (DEAP), *Phys. Rev. D* **100**, 022004 (2019).
- [8] R. Agnese *et al.* (SuperCDMS), *Phys. Rev. Lett.* **112**, 041302 (2014).
- [9] H. Jiang *et al.* (CDEX), *Phys. Rev. Lett.* **120**, 241301 (2018).
- [10] A. Abdelhameed *et al.* (CRESST), *Phys. Rev. D* **100**, 102002 (2019).
- [11] C. Amole *et al.* (PICO), *Phys. Rev. Lett.* **118**, 251301 (2017).
- [12] Y. Meng *et al.* (PandaX), *Phys. Rev. Lett.* **127**, 261802 (2021).
- [13] E. W. Kolb and M. S. Turner, *The Early Universe*, Vol. 69 (1990).
- [14] L. J. Hall, K. Jedamzik, J. March-Russell, and S. M. West, *JHEP* **03**, 080, arXiv:0911.1120 [hep-ph].
- [15] C. Cheng *et al.* (PandaX), *Phys. Rev. Lett.* **126**, 211803 (2021).
- [16] R. Essig, J. Mardon, and T. Volansky, *Phys. Rev. D* **85**, 076007 (2012).
- [17] R. Essig, A. Manalaysay, J. Mardon, P. Sorensen, and T. Volansky, *Phys. Rev. Lett.* **109**, 021301 (2012).
- [18] A. Aguilar-Arevalo *et al.* (DAMIC), *Phys. Rev. Lett.* **123**, 181802 (2019).
- [19] T. Emken, R. Essig, C. Kouvaris, and M. Sholapurkar, *Journal of Cosmology and Astroparticle Physics* **2019** (09), 070.
- [20] R. Essig, M. Fernandez-Serra, J. Mardon, A. Soto, T. Volansky, and T.-T. Yu, *JHEP* **05**, 046, arXiv:1509.01598 [hep-ph].
- [21] R. Essig, T. Volansky, and T.-T. Yu, *Phys. Rev. D* **96**, 043017 (2017), arXiv:1703.00910 [hep-ph].
- [22] H. Zhang *et al.* (PandaX), *Sci. China Phys. Mech. Astron.* **62**, 31011 (2019).
- [23] Z. Qian *et al.* (PandaX), *Journal of High Energy Physics* **147**, 10.1007/JHEP06(2022)147 (2022).
- [24] C. He, J. Liu, X. Ren, X. Shang, X. Wei, M. Wang, J. Yang, J. Yang, Y. Yang, G. Zhang, and Q. Zheng, *Journal of Instrumentation* **16** (12), T12015.
- [25] X. Chen, C. Cheng, M. Fu, F. Giuliani, J. Liu, X. Lu, X. Ji, Z. Qian, H. Qiao, Q. Wang, J. Xia, P. Xie, Y. Yao, and H. Zhang, *Journal of Instrumentation* **16** (09), T09004.
- [26] L. Zhao, X. Cui, W. Ma, Y. Fan, K. Giboni, T. Zhang, J. Liu, and X. Ji, *Journal of Instrumentation* **16** (06), T06007.
- [27] X. Wang, S. Li, Y. Ju, Z. Lei, J. Liu, X. Ji, X. Tang, and Y. Gou, *Review of Scientific Instruments* **92**, 093905 (2021).
- [28] W. Ma *et al.* (PandaX), arXiv:2207.04883.
- [29] Such background can also emerge from the gate electrode, but is significantly suppressed by our data selection based on the  $S2$  width.
- [30] Under cut1,  $S2s$  in set 2 are stretched due to a slightly different  $S2$  gain of this dataset.
- [31] E. Aprile *et al.* (XENON), *Phys. Rev. Lett.* **123**, 251801 (2019).
- [32] P. Agnes *et al.* (DarkSide-50), (2022), arXiv:2207.11968.
- [33] R. Essig, T. Volansky, and T.-T. Yu, *Phys. Rev. D* **96**, 043017 (2017).
- [34] O. Abramoff *et al.* (SENSEI), *Phys. Rev. Lett.* **122**, 161801 (2019).
- [35] E. Aprile *et al.* (XENON), *Phys. Rev. Lett.* **126**, 091301 (2021).
- [36] D. Akerib *et al.* (LUX), *Phys. Rev. Lett.* **118**, 021303 (2017).
- [37] P. Agnes *et al.* (DarkSide-50), (2022), arXiv:2207.11966.
- [38] M. Szydagis, J. Balajthy, J. Brodsky, J. Cutter, J. Huang, E. Kozlova, B. Lenardo, A. Manalaysay, D. McKinsey, M. Mooney, *et al.*, Zenodo: Geneve, Switzerland (2018).
- [39] M. Szydagis, *Bulletin of the American Physical Society* (2022).
- [40] D. S. Akerib *et al.* (LUX), *Phys. Rev. D* **96**, 112011 (2017), arXiv:1709.00800 [physics.ins-det].
- [41] D. Baxter, I. Bloch, E. Bodnia, X. Chen, J. Conrad, P. Di Gangi, J. Dobson, D. Durnford, S. Haselschwardt, A. Kaboth, *et al.*, *The European Physical Journal C* **81**, 1 (2021).

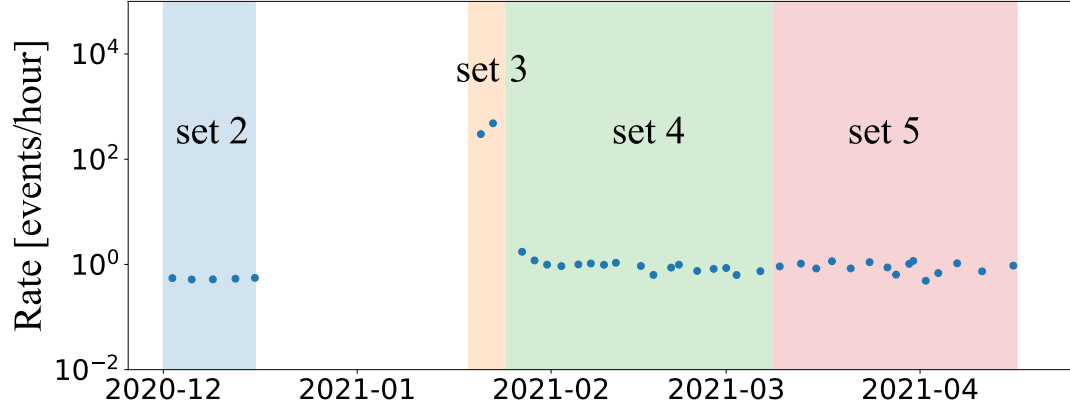


FIG. 6. The time evolution of the  $S_2$  (40-60 PE) event rate under cut1. The set 3 is dominated by the MD background. The average rate of set 4 and set 5 are about 1.7 times higher than that of set 2.

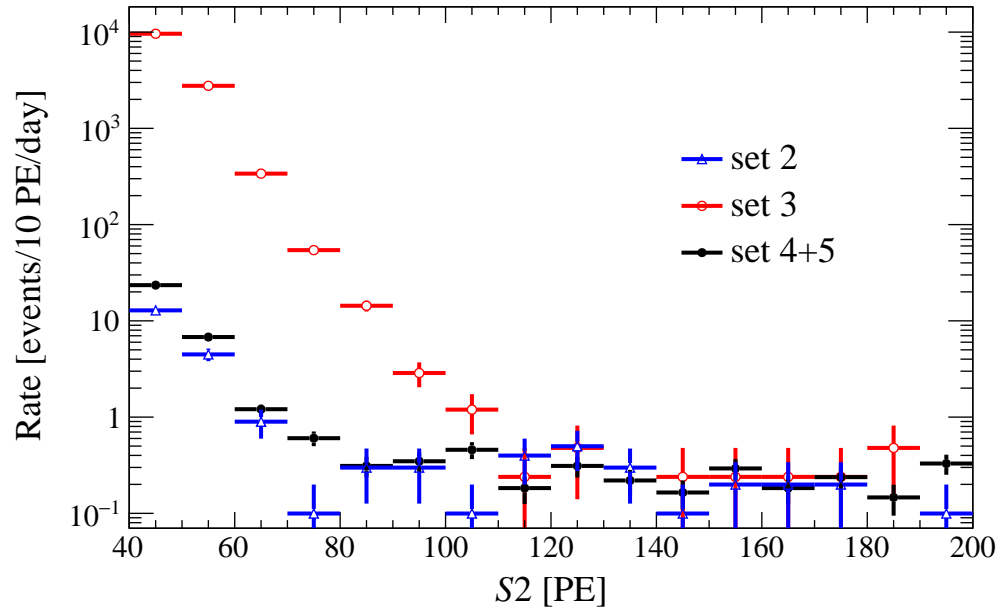


FIG. 7. The  $S_2$  spectra of set 2 (blue dots), set 3 (red circles), and set 4+5 (black dots). The  $S_2$ s in the set 2 are scaled so that the  $S_2$  gain is consistent with set 4+5 when performing MD background estimation.

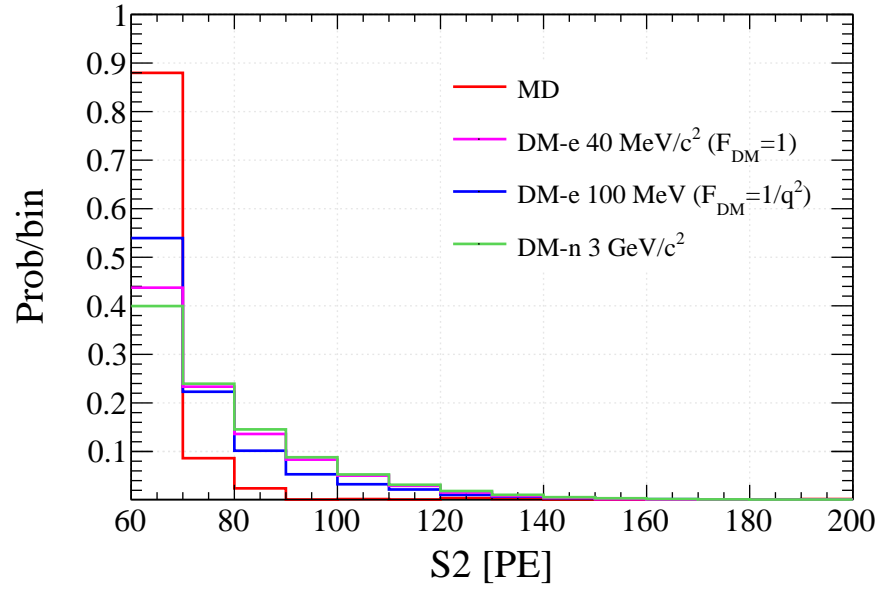


FIG. 8. The comparison of the  $S2$  spectra of MD (red), DM-e  $40 \text{ MeV}/c^2$  ( $F_{DM} = 1$ ) (purple), DM-e  $100 \text{ MeV}/c^2$  ( $F_{DM} = 1/q^2$ ) (blue), and DM-n  $3 \text{ GeV}/c^2$  (green).